Fast Diagnostic Methods for Large-Scale Full-Satellite Antenna Measurements

ESTEC Contract No. AO/1-9352/18/NL/AF

ESR: Executive Summary Report

Provided by: TICRA, Denmark

December, 2021 S-1675-ESR

Revision 1.0

TICRA
LANDEMÆRKET 29 · DK-1119 COPENHAGEN K DENMARK
TELEPHONE +45 33 12 45 72
E-MAIL ticra@ticra.com http://www.ticra.com

VAT REGISTRATION NO. DK-1055 8697
TICRA FOND, CVR REG. NO. 1055 8697

Issue	Date	Record of changes	Author
1.0	2021-12-09	Initial revision.	Andreas Ericsson, Oscar Borries, Martin Haulund Gæde, Erik Jørgensen, Peter Meincke

Fast Diagnostic Methods for Large-Scale Full-Satellite Antenna Measurements

Executive Summary Report
ESA Contract No. AO/1-9352/18/NL/AF

***Abstract*—This document summarises the work performed within the ESA Contract No. AO/1-9352/18/NL/AF. It discusses the development of a fast source reconstruction method suitable for antenna diagnostic applications of radiating structures on electrically large platforms. During the activity, a number of different numerical methods have been investigated, both from a theoretical perspective and from an implementation standpoint, in order to develop a source reconstruction method that is significantly faster than previous methods. The final algorithm utilizes a combination of matrix free methods and a novel implementation of a recent reformulation of the inverse electromagnetic scattering problem. Furthermore, the source reconstruction problem is solved using a higher order Method of Moments (MoM) discretization. This method achieves asymptotically better scaling the previously possible, and in particular the memory use is substantially lower than was previously possible. Results from two example cases are presented where the new method is compared to the current commercial state-of-the-art solver in DIATOOL 1.1, and significant improvements are observed in terms of computation times and memory requirements.**

***Index Terms*—Source reconstruction, antenna diagnostics, Calderón method**

I. Introduction

Source reconstruction is a highly relevant topic that has attracted much attention throughout the past decades in applications such as antenna diagnostics [1]–[3], near-field to far-field transformation and filtering [4], [5], antenna placement investigations [6] and performance analyses of 5G devices [7]. While the applications vary, the fundamental challenge is to find the currents that radiate a specific electromagnetic field.

The electromagnetic source reconstruction problem is a linear inverse problem based on finding currents with known location that radiate a given complex vector field [8]. The problem is naturally formulated in terms of integral equations based directly on Maxwell's equations. For applications with diagnostics purposes, the equations should be augmented with Love's condition of zero fields inside a surface enclosing the sources, such that the sought currents provide a unique solution [9] that represents the actual physical currents on the structure.

Inverse equivalent surface current solvers is the tool that is used to process near-field or far-field measurement data in order to reconstruct the fields or currents in the extreme near-field region of the radiating structure. A common limitation with most inverse equivalent surface current solvers to date is that their computational requirements have less desirable scaling properties in comparison to their forward-solver (radiation problem) counter-parts in terms of frequency, electrical size of the scatterer and the amount of input data required to solve the problem. Much work have been presented to date that attempts to mitigate these limitations [10]–[12], but for diagnostics purposes, the fundamental challenges regarding the required memory and computation time have remained.

In this activity, the goal has been to develop an accelerated source reconstruction method suitable for carrying out antenna diagnostics on very large problems, such as a science instrument located on a satellite platform. The heritage of TICRA in terms of a state-of-the-art Method of Moments (MoM) solver, based on higher-order basis functions and higher-order mesh elements [13], together with innovative regularization techniques [14], have been used as a stepping stone to accelerate the development of new improved source reconstruction methods.

The main driver for the improved results in this activity is that of a projection operator based on Calderón operators as first presented in [15]. It has been shown that by using a Calderón projection it is assessed that the achieved solution yields the correct currents from a physical point of view. However, the numerical implementation described in [15] can be improved substantially upon, in particular in terms of the projection operation itself.

In order to achieve acceptable performance when reconstructing currents on electrically large structures, matrix-free representations of the relevant operators are necessary. Using matrix-free operators lead to a number of challenges, in particular regarding the memory/computational time trade-off. The specific implementation shown in this paper achieves drastic improvements, around two orders of magnitude, in terms of memory requirements and computational time, without sacrificing solution accuracy compared to previously presented inverse source reconstruction methods.

The paper is organised as follows, in Section II the theory and numerical implementation of the proposed method are presented. Then, In Sections III–IV an overview is given of the DIATOOL source reconstruction software framework and GUI in which the method has been integrated. After that, the results from two source reconstruction application cases are presented in Section V, followed by some concluding remarks in Section VI.

II. Theory and Implementation

The basic electromagnetic concept involved in reconstructing currents is the equivalence principle, which states that the sources and scatterers enclosed inside a reconstruction surface

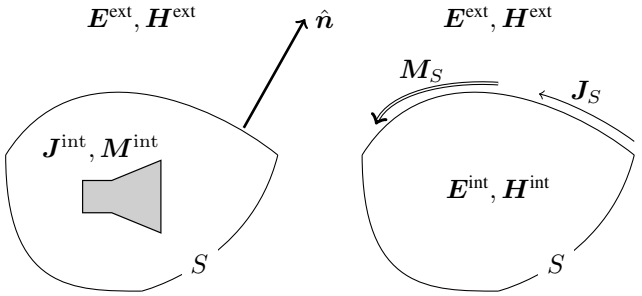

Fig. 1: The equivalence principle for an imaginary closed surface S: original problem (a) and equivalent problem (b). Introducing surface current densities on S, $\boldsymbol{J}_S$ and $\boldsymbol{M}_S$, which radiate the fields $\boldsymbol{E}^{\text{ext}}$ and $\boldsymbol{H}^{\text{ext}}$ outside S such that the sources inside S can be removed.

(RS) S, here labelled $\boldsymbol{M}^{\text{int}}$, $\boldsymbol{J}^{\text{int}}$, can be replaced by an equivalent set of surface current densities $\boldsymbol{M}_S, \boldsymbol{J}_S$ on S, such that these currents radiate the same fields $\boldsymbol{E}^{\text{ext}}, \boldsymbol{H}^{\text{ext}}$ outside the surface. This concept is illustrated in Fig. 1. Consequently, $\boldsymbol{E}^{\text{ext}}, \boldsymbol{H}^{\text{ext}}$ and the currents on the surface are related by the outward unit normal vector $\hat{\boldsymbol{n}}$ [16]

$$\boldsymbol{J}_S = \hat{\boldsymbol{n}} \times (\boldsymbol{H}^{\text{ext}} - \boldsymbol{H}^{\text{int}}), \tag{1}$$

$$\boldsymbol{M}_S = -\hat{\boldsymbol{n}} \times (\boldsymbol{E}^{\text{ext}} - \boldsymbol{E}^{\text{int}}). \tag{2}$$

Based on these surface current densities, a data equation can be set up, linking measurements and the equivalent currents. This data equation is represented on discretized form by the relation

$$\overline{\overline{A}}\bar{x} = \bar{b}, \tag{3}$$

where $\overline{\overline{A}}$ is a matrix representing the radiation from the unknown currents $\bar{x}$ on S that generate the measured fields in $\bar{b}$.

The key challenge is that the currents determined by a solution to (3) are non-unique due to the presence of the $-\boldsymbol{H}^{\text{int}}$ and $-\boldsymbol{E}^{\text{int}}$ terms in (1)–(2). To overcome this problem Love's equivalent current condition [9] of zero fields inside of S ($\boldsymbol{H}^{\text{int}} = \boldsymbol{E}^{\text{int}} = 0$) is considered. This condition is formulated on discretized form as

$$\overline{\overline{L}}\bar{x} = 0, \tag{4}$$

where again $\bar{x}$ are the unknown currents and $\overline{\overline{L}}$ is the matrix representation of Love's condition. Most previous works are based on solving the coupled system of equations in (3) and (4). However, this approach is computationally expensive to solve in general, and since regularization is needed to balance the two conditions, a matrix-free approach is inefficient.

An alternative approach was suggested recently in [15], where a Calderón projection is used to restrict the solution space to the space spanned by the Love currents. More specifically, a Calderón pre-conditioner was formulated for the iterative solution of the inverse problem. This approach implies that we can find the unique Love currents by starting with any set of the non-unique currents (3), and then simply compute and subtract the contribution from the unwanted interior fields. This so called Calderón projection is discretized to

$$\bar{x}^{\text{Love}} = \overline{\overline{T}}\bar{x}, \tag{5}$$

where $\bar{x}$ are the initial reconstructed currents, $\bar{x}^{\text{Love}}$ are the sought after currents that fulfil Love's condition, and $\overline{\overline{T}}$ is similar to $\overline{\overline{L}}$ except for some differences in the underlying mathematical expressions. Although the non-uniqueness is solved by enforcing (4), or by applying the mapping (5), the problem is still ill-posed. A regularization scheme is therefore needed to obtained a stable solution.

Based on the theoretical discussion so far, the mathematical problem to solve can be formulated as

$$\min_{\bar{x}} \|\overline{\overline{A}}\bar{x} - \bar{b}\|_2, \tag{6}$$

$$\text{s.t. } \overline{\overline{L}}\bar{x} = 0, \tag{7}$$

and with the assumption that $\overline{\overline{L}}\overline{\overline{T}}\bar{x} = 0$, i.e. the range of $\overline{\overline{T}}$ coincides with the null-space of $\overline{\overline{L}}$. The Calderón mapping allows us to restate this problem simply as a preconditioned Least Squares problem

$$\min_{\bar{z}} \|\overline{\overline{A}}\overline{\overline{T}}\bar{z} - \bar{b}\|_2, \tag{8}$$

yielding the solution $\bar{x} = \overline{\overline{T}}\bar{z}$. The problem (8) can be solved in a number of ways, and in this work a novel solution procedure is proposed.

The solution procedure consists of using the Conjugate Gradient Least Squares (CGLS) method as an iterative procedure to solve the system $\|\overline{\overline{A}}\bar{x} - \bar{b}\|_2$, and then applying $\overline{\overline{T}}$ to that solution to make sure the solution fulfils Love's condition. After the $\overline{\overline{T}}$ projection, a few additional CGLS iterations are taken to slightly reduce the residual of the system. Specifically, the procedure has three steps:

1) Solve $\bar{y} = \arg\min_{\bar{x}} \|\overline{\overline{A}}\bar{x} - \bar{b}\|_2$ using CGLS.
2) Compute $\bar{z} = \overline{\overline{T}}\bar{y}$.
3) Take a few iterations of CGLS applied to the problem $\bar{y} = \arg\min_{\bar{x}} \|\overline{\overline{A}}\bar{x} - \bar{b}\|_2$, with starting guess $\bar{x}_0 = \bar{z}$.

This procedure has several advantages. First and foremost, only one matrix-vector product with $\overline{\overline{T}}$ is necessary which means that $\overline{\overline{T}}$ does not need to be stored. Additionally, the only matrix to be applied multiple times is $\overline{\overline{A}}$, and many efficient algorithms exist for computing the action of this matrix and its hermitian. Crucially, all matrix multiplications with $\overline{\overline{A}}$ are done in this work using so-called fast methods, i.e. methods that scale at most as $\mathcal{O}(a \log b)$ where $a = b = \max\{M, N\}$, and $M/2$ is the number of measurement data points and N is the number of unknowns. This means that both memory and computational time scales as $\mathcal{O}(N \log N)$ or $\mathcal{O}(M \log M)$, which is asymptotically better than all previously published methods.

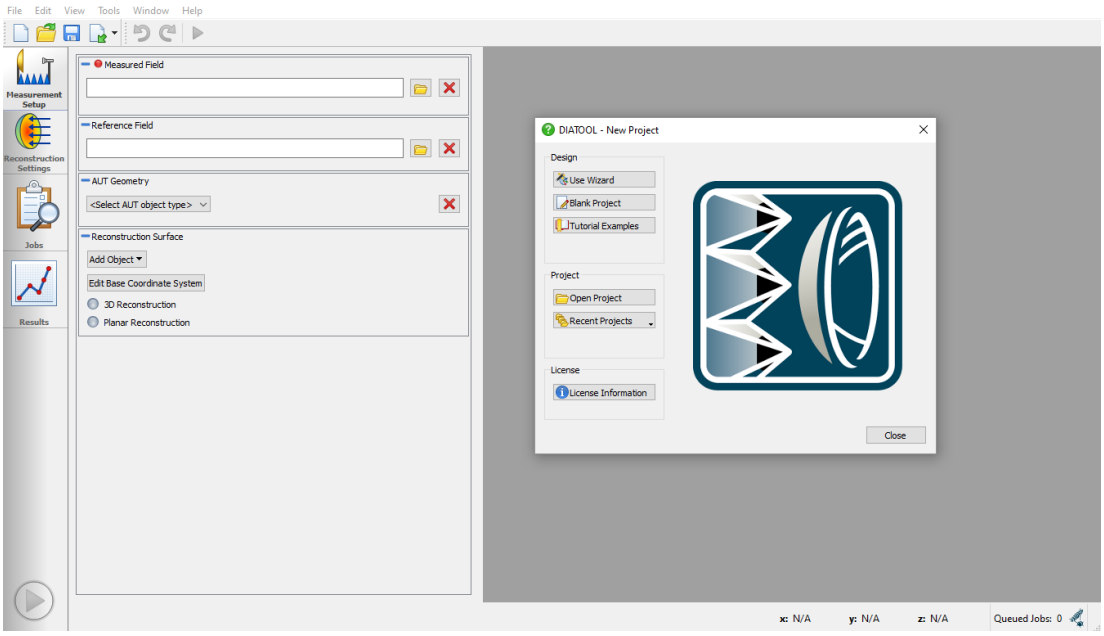

Fig. 2: The DIATOOL software framework.

III. DIATOOL Software Technical Description

The new source reconstruction solver has been integrated in the TICRA DIATOOL software framework. In this section, a technical description is presented of DIATOOL, which consists of two main components: A Graphical User Interface (GUI) and a back-end module. The GUI assists the user in:

1) Importing the input data, such as measured field, and, when available, reference field and AUT geometry.
2) Defining the reconstruction surface by choosing among a set of predefined geometries, or by reading an input file.
3) Selecting the reconstruction algorithm and launching the computation invoking the back-end module.
4) Visualizing the results computed by the back-end module.

The back-end module performs the field and current reconstruction as well as number of tasks related to project management, i.e. logging, file input/output, 3D drawing, and license management. A list of the technical specifications can be found in [17].

A. Reconstruction methods

Two families of algorithms are available in DIATOOL that are used to compute the near-field or the currents on the antenna surface. The first one, in the following called the "3D reconstruction" technique, are inverse MoM algorithms based on higher-order basis functions and curved geometry modeling. The novel algorithm developed in this activity is one of the available solvers under the 3D reconstruction technique. This technique makes it possible to reconstruct the field on arbitrary 3D surfaces enclosing the AUT. The second one, in the following referred to as the "planar reconstruction" technique, is a modal approach involving a spherical-to-plane wave transformation, allowing the field to be reconstructed on planar surfaces in front of or around the AUT, see [23] for details. Both techniques provide a theoretically unlimited resolution in the reconstructed field, whereas the resolution achieved in practice is limited by the noise level of the measured data. A brief description of the two methods is given in the following.

The capabilities of the 3D reconstruction algorithm can be summarized as follows:

1) Input measured field (in amplitude and phase) on any acquisition surface, including truncated and irregular surfaces.
2) Reconstruction of equivalent electric and magnetic currents on the antenna surface or an arbitrary surface enclosing it.
3) Possibility of assigning special properties to various parts of the mesh: Patches can be marked for zero radiation. The currents on these patches are included in the reconstruction process but the radiation is cancelled when computing secondary radiation patterns. Patches can also be marked as perfectly conducting. The magnetic currents are forced to zero on these patches, which reduces the computational requirements.
4) Applicable to both electrically small and large antennas.
5) Computationally more demanding than the planar reconstruction algorithm.
6) Resolution limited by the antenna electrical size and the dynamic range of the measured input field. It is often better than $\lambda/2$.

The capabilities of the planar reconstruction algorithm can be summarized as follows:

1) Input measured field (in amplitude and phase) on a full sphere.
2) Field reconstruction on a plane or combination of planes, .e.g., a box.
3) Applicable to both electrically small and large antennas.
4) Fast computation with low memory requirements.
5) Resolution limited by the antenna electrical size and the dynamic range of the measured input field. It is often better than $\lambda/2$.

B. Input data

This section describes the various files that need to be read or defined before running a field reconstruction.

1) Measured field: The file containing the measured field can be read in the following file formats:

1) TICRA cut or TICRA grid (.cut, .grd)
2) TICRA SWE file (.sph, .swe)
3) Electromagnetic Data Exchange (EDX) (.edx). The file may contain either a SWE or measured field samples
4) ASCII file exported from MI-Technologies 3000 software (.txt)
5) ASCII file exported from NSI 2000 Professional software (.asc)

The planar algorithm works with a SWE and field samples in a regular grid on a spherical surface. The 3D algorithm works with a SWE, near- or far-field data on a spherical surface, as well as near-field data on planes and cylinders. The field data may be arranged in a regular or an irregular grid. For a description of the EDX format please see [24].

2) Reference field: The reference field is an optional input file. It represents the field that the antenna should radiate where no errors are present and is typically a field computed by simulation. The reference field option allows one to directly compare the equivalent currents reconstructed from the measured field with the ones reconstructed from the reference field. The reference field may be specified in the same file formats as described for the input data.

3) AUT geometry: The AUT geometry is an optional input file. If provided, it enables automatic fitting of the reconstruction surface to the AUT geometry. In addition, it allows to detect misalignment of the measurement coordinate system and the surface of reconstruction, or intersection of the AUT with the reconstruction surface. The AUT geometry can be imported either as a CAD file in STEP or IGES format, or as a meshed geometry.

4) Reconstruction surface: DIATOOL reconstructs fields and currents on arbitrarily shaped closed surfaces enclosing the antenna as well as on truncated planes. The available reconstruction surfaces depend on the reconstruction algorithm, i.e. the 3D algorithm only allows closed surfaces while the planar algorithm only allows truncated planes.

The reconstruction surface can be specified by simple canonical shapes as well as arbitrary surfaces imported from a file.The following reconstruction surfaces are available:

1) Surface imported from a CAD file
2) Mesh of a closed surface
3) Body revolution defined by a piecewise linear curve
4) Ellipsoid
5) Elliptical cylinder
6) Box
7) Truncated Plane

C. Coordinate systems

The measured field, AUT and reconstruction surface are defined relative to their own coordinate system. Each coordinate system is given in a base coordinate system, which, for the measured field and AUT, coincides with the global coordinate system. The base coordinate system of each reconstruction surface can be edited, i.e. it can be translated and rotated. The orientation can be defined

1) In the Cartesian system, by two orthogonal vectors along any two of the three coordinate vectors
2) In the so-called GRASP notation, by the three angles θ, ϕ and ψ
3) In Euler notation, by the three angles α, β and γ

D. Output data

The results computed by DIATOOL are visualized in the Results Manager, see Section IV-G for a detailed description. Several plots are available, depending on the type of input data provided to DIATOOL, and the chosen reconstruction algorithm.

IV. DIATOOL Software GUI

The DIATOOL GUI is composed by a Measurements Setup editor, a Reconstruction Settings editor, a Jobs Manager and a Results Manager. Each of these components will be now briefly described.

A. Measurements Setup editor

The Measurements Setup Editor lets the user set up the reconstruction problem manually, without going through the wizard. An example of Measurements Setup Editor is shown in Fig. 3. In the Measurements Setup Editor the user defines the

- Measured field
- Reference field (optional)
- AUT geometry (optional)
- Reconstruction surface

B. Measured field and Reference field

A measured field or a reference field is read into DIATOOL by browsing to the location where the file is located. Depending on the format and type of the input file that will be read, different entries will then appear in the Editor to allow the user to input remaining information that is not available in the file. For instance, some file formats do not specify the measurement frequency. If the input file is a file with field data in polar cuts, the user has the possibility of computing a SWE on-the-fly and use this SWE in the reconstruction algorithm. Depending on the type of file loaded as measured field, DIATOOL will show a red or a green light and a short explanation, to

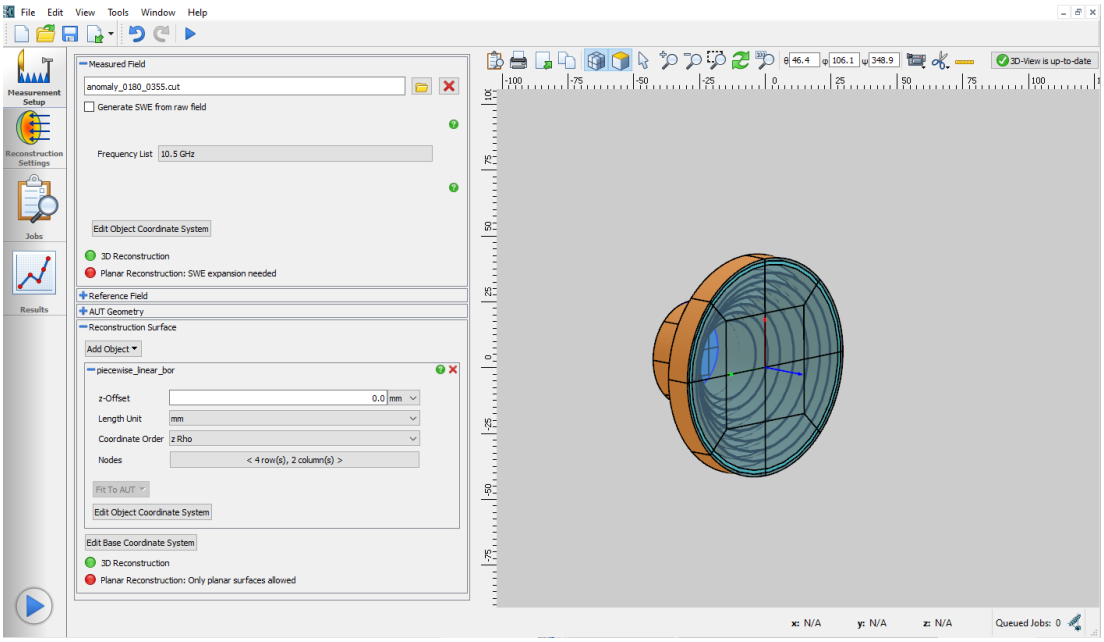

Fig. 3: Typical DIATOOL Measurements Setup Editor.

indicate whether both reconstruction algorithms or only the 3D algorithm can be used. If the measured input field is not given by a SWE or field data in polar cuts, only the 3D algorithm can be used. However, the user has the possibility to generate, with the help of cubic interpolation, a SWE compatible file to be used as input file.

C. AUT geometry

The AUT geometry is defined by reading a CAD file or a mesh file. Red and green lights will indicate possible compatibility issues with the two reconstruction algorithms.

D. Reconstruction surface

The reconstruction surface is chosen by selecting one of the possible surfaces mentioned in Section III-B4 . Depending on the measured input field and the chosen reconstruction surface, DIATOOL will indicate possible compatibility issues with the two reconstruction algorithms.

The chosen reconstruction surface will automatically be shown in the canvas on the right side of the Object window. Here DIATOOL shows by default the reconstruction surface, all defined coordinate systems and the AUT geometry (if present). The 3D radiation pattern of the measured field can also be shown, which allows the user to easily detect possible misalignments. The user also has the possibility to zoom in and out, rotate freely the objects or choose some predefined viewing planes. Moreover, the user can assign special electrical properties to various parts of the reconstruction surface, i.e., ”PEC” or ”zero radiation”.

E. Reconstruction Settings editor

The Reconstruction Settings editor allows the user to choose the reconstruction method and change the default setup. By default, the outputs computed by DIATOOL are the reconstructed currents and fields on the surface of reconstruction. However, the user may request additional field output in which case the radiation from the reconstructed currents is computed in the user-specified cut or grid.

If the 3D reconstruction is chosen, the user may enable zero-padding of the measured/reference input field in the directions where the field is not provided. This can be used when the measured field is truncated in directions where the field is expected to be negligible. In addition, the user can adjust the ”Performance Optimization” by choosing between ”normal”, ”small scale” and ”high accuracy”. The default ”normal” corresponds to using the newly implemented Calderón method and this will be significantly faster and use less memory than the other settings. The ”small scale” setting corresponds to using the previous state-of-the-art standard-form conjugate gradient least squares (SCGLS) method. Finally, when dealing with noise-free data, the high-accuracy setting may provide a more accurate reconstruction, at the expense of a longer computation time and larger memory consumption.

If the planar reconstruction is chosen, the user may select between three types of filtering:

- No filter. This implies that only the visible spectrum will be used.
- Hann filter. This may reduce the ripples in the reconstructed field, at the expenses of a slightly larger spatial field distribution on the reconstruction plane.
- Evanescent waves. If the antenna is electrically small and if measured/reference fields with high precision are available, DIATOOL can recover part of the invisible spectrum by taking into account evanescent waves.

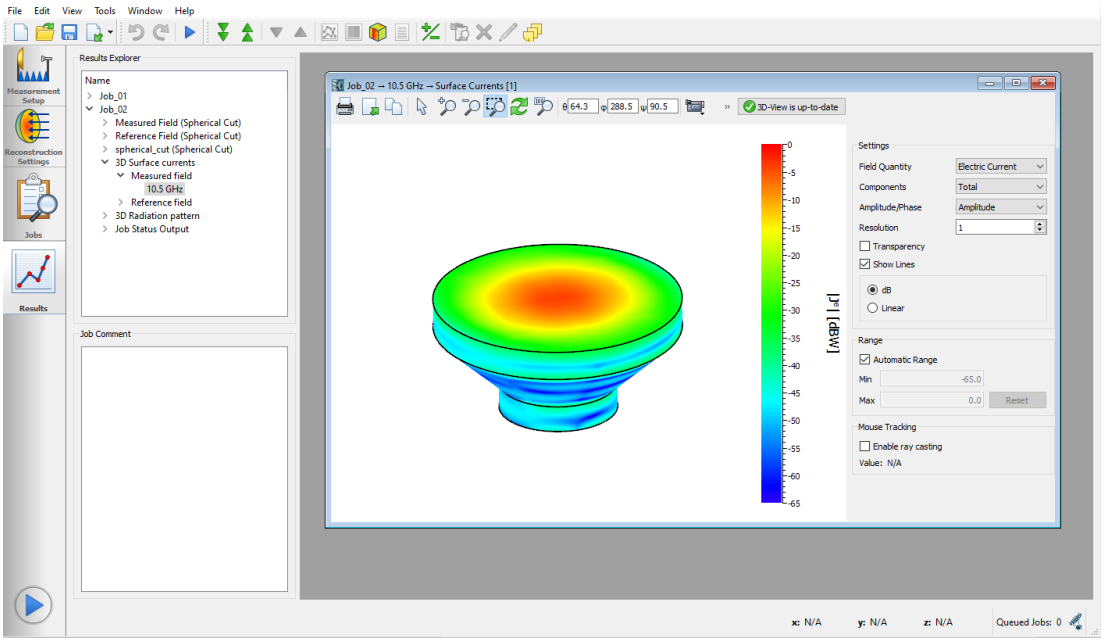

Fig. 4: A typical 3D surface currents plot.

F. Jobs Manager

The Jobs Manager window is a job queue showing completed, running, and pending jobs. During the execution, the user can inspect how the job progresses. For the 3D reconstruction, the equivalent signal to noise ratio (SNR) of the reconstructed currents will be shown. The equivalent SNR is a measure of the noise present in the input field as well as of the errors that come from the 3D algorithm itself, such as mesh discretization and solution of the inverse problem. The equivalent SNR provides useful information about the accuracy of the solution.

G. Results Manager

The Results Manager collects all results computed by DIATOOL. In addition, the Results Manager may be used to delete Jobs or to revert to a previous configuration.
The two major parts of the Results Manager are:

- A tree view to the upper left, in the so-called Results Explorer. In the tree view results are sorted by the job to which they belong. Each entry in the tree contains a number of sub-entries depending on the job. Double-clicking on the entry leads to a plot or a listing of the calculated result.
- A plot canvas to the right. The plot canvas may contain an unlimited number of plots, with results from the present job, or comparison of results from different jobs. The plots are saved to the project files, and consequently re-plotted when the project is re-opened.

Both reconstruction algorithms provide a 3D plot of the reconstructed surface currents/tangential fields. Electric and magnetic currents, as well as tangential E-field and H-field can be chosen, see for example Fig. 4. These are plotted in amplitude and phase. A 3D radiation pattern is plotted only when the 3D reconstruction algorithm is used. The pattern is computed by integrating the reconstructed equivalent currents. A rich set of customization options are available in the results manager. In addition, curves can be cut and pasted as well as exported to ASCII-files as comma- or tab-separated values. Finally, all plots can be printed or exported as graphics files.

V. Application Case Results

Two application cases are presented where the novel 3D reconstruction method solver is put to the test. The first case consists of simulated data of a 10 GHz reflector antenna on a satellite platform. There are a number of advantages associated with using simulated data as input to the source reconstruction software for testing purposes. For example, noise can easily be added manually to the data to synthesise any level of measurement noise, and the errors in the reconstructed fields and currents can be computed from comparison with known near-field data. This case will test if the presented method can handle source reconstruction of extremely large problems. The second case consists of measured data of a 664 GHz feed horn from the meteorological operational satellite second generation (MetOp-SG) ice cloud imager in [25]. This case will test how well suited the presented method is for high frequency source reconstruction applications.

A. Reflector antenna on satellite platform

A simplified model of the OHB SmallGeo satellite platform with three reflector antennas was implemented in TICRA Tools. The platform has the outer dimensions 2.6 m x 1.6 m x 3.1 m and is presented in Fig. 5. The reflectors, which are labelled 1, 2 and 3 in Fig. 5, are each illuminated by a corrugated horn antenna, located at the reflector focal point,

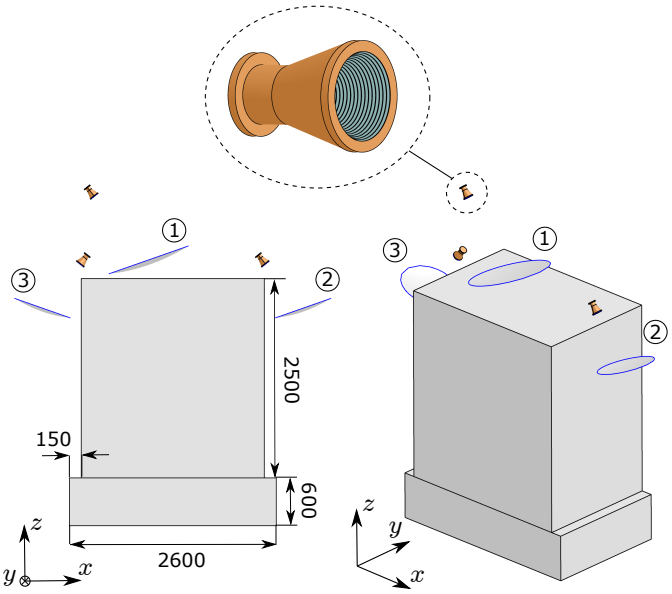

Fig. 5: Application case 1, OHB SmallGeo satellite platform with three reflector antennas illuminated by corrugated feed horns, seen from two different perspectives.

operating at 10 GHz with an illumination tapering of -12 dB at the edge of the reflector. The feed antennas can easily be scaled in frequency and operate in either linear polarisation (LP) or circular polarisation (CP).

In this work, only the horn illuminating reflector 2 is active and radiates in LP in the offset direction. The illuminated reflector has a diameter and focal length of 0.7 m and an offset of 0.49 m. The far-field of the complete geometry was computed in TICRA Tools using the MoM/MLFMM solver in ESTEAM and exported as a full sphere cut with a sampling spacing of 0.1° in θ and in ϕ, resulting in 6 481 800 sampling points in total. A normal distributed random noise level corresponding to a signal-to-noise ratio (SNR) of 60 dB was added to the data so synthesise a real measurement scenario.

A box enclosing the platform and the reflectors with the measures 4.1 m x 1.8 m x 3.6 m was used as RS. The reconstructed currents on the RS were computed based on the total field from the feed and the platform with reflectors. The computational details of the reflector on platform source reconstruction case are presented in Table I. In summary, the problem consists of 3 229 688 higher order (HO) unknowns (equivalent to about 13 million Rao-Wilton-Glisson (RWG) unknowns), requires 60.2 GB random access memory (RAM) and finishes in a little over 4 h when analysed on a workstation computer with a Cascade Lake CPU with 32 physical cores. We stress that this is substantially lower than previously reported results in the literature, and in particular the RAM use is actually comparable to the RAM required for the forward problem, a remarkable conclusion.

The antenna geometry enclosed by the RS and the magnitude of the reconstructed equivalent electric current density are presented in Fig. 6. The centre feed horn is not enclosed

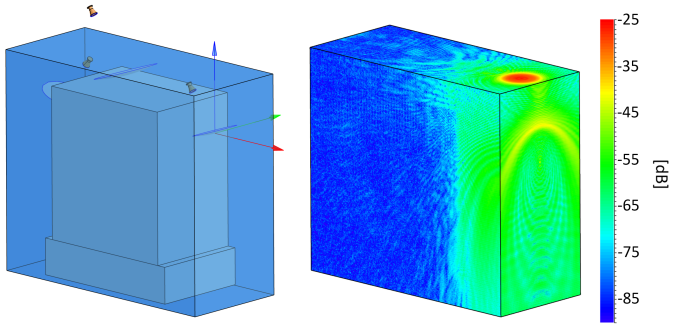

Fig. 6: Application case 1 with a box RS (left) and the magnitude of the reconstructed electric current density (right).

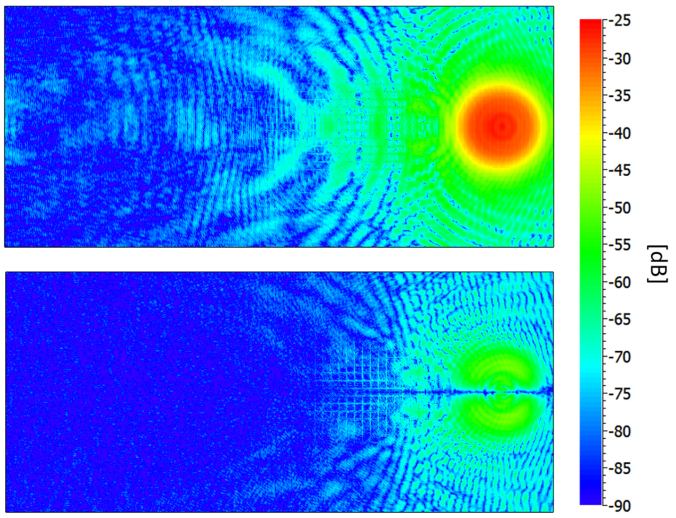

Fig. 7: Application case 1 reconstructed electric current density. The co-polarisation currents are presented at the top and the cross-polarisation currents at the bottom.

by the RS since the scattering effect from this object on the radiated far-field was negligible. The reflector radiation is clearly visible and looks as expected in the reconstructed currents. A more detailed representation of the reconstructed currents is presented in Fig. 7, where the co-polarisation and cross-polarisation of the electric current density are viewed from the main beam direction of the reflector far-field.

To validate that the reconstructed currents are in fact the sought after unique physical currents, the scattered field from the platform and the reflectors was used as input for source reconstruction on the same RS that what was used for the total field. From this second set of reconstructed currents the root-mean-square error (RMSE) was computed in relation to the corresponding forward MoM currents computed in TICRA Tools ESTEAM. The RMSE of the electric current density is defined as

$$\mathrm{RMSE}_J = \sqrt{\frac{\sum_{i=1}^{N_{\mathrm{RMS}}} \left| \boldsymbol{J}_S^{\mathrm{rec}}(x_i, y_i, z_i) - \boldsymbol{J}_S^{\mathrm{ref}}(x_i, y_i, z_i) \right|^2}{\sum_{i=1}^{N_{\mathrm{RMS}}} \left| \boldsymbol{J}_S^{\mathrm{ref}}(x_i, y_i, z_i) \right|^2}}, \tag{9}$$

where $\boldsymbol{J}_S^{\mathrm{rec}}(x_i, y_i, z_i)$ and $\boldsymbol{J}_S^{\mathrm{ref}}(x_i, y_i, z_i)$ are the the recon-

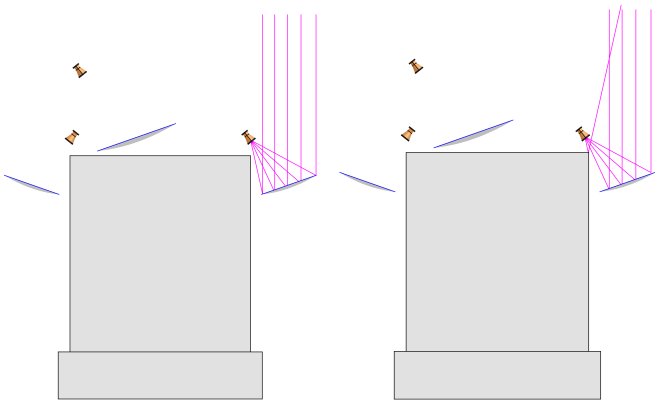

(a) (b)

Fig. 8: Nominal antenna setup (a) and a platform blockage error introduced to the radiating antenna (b).

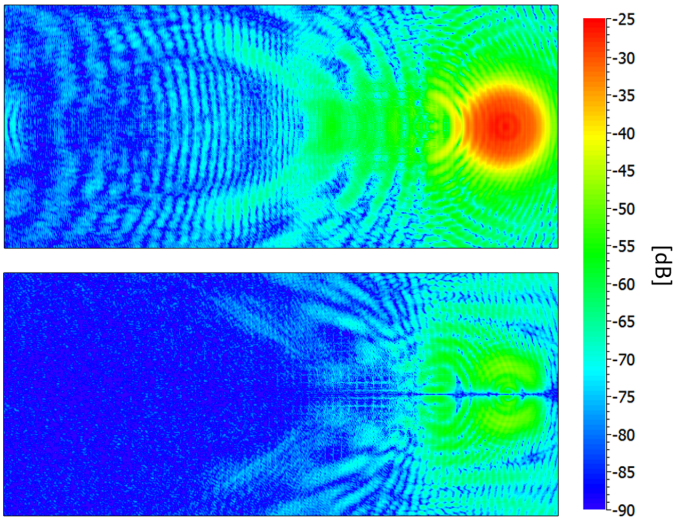

Fig. 9: Reconstructed electric current density where a reflector illumination blockage defect has been introduced. The co-polarisation currents are presented at the top and the cross-polarisation currents at the bottom.

structed and reference MoM current densities evaluated at the points in space (x_i, y_i, z_i), and N_{RMS} is the number of equally spaced evaluation points on the RS. The definition in (9) was also used to evaluate the corresponding RMSE of the reconstructed magnetic current density. A worst-case RMSE of 6.6 % was computed, which is acceptable in relation to the requirements specified in the activity of RMSE $< 10\,\%$.

From the reconstructed currents the electric and magnetic fields can be computed anywhere in space outside of the RS. As an additional validation test, the reconstructed far-fields were computed and compared to the input far-field data provided to the algorithm. The far-field was computed with the sampling $\theta = [0, 180]^\circ$, $N_\theta = 1001$, $\phi = [0, 315]^\circ$, $N_\phi = 8$. The resulting far-field RMSE was $< 0.5\,\%$ which indicates that the input far-field was successfully reconstructed.

The synthetic measurement model in TICRA Tools enables the possibility to introduce different types of antenna defects to be detected. The feed and reflector of antenna 2 were translated 50 mm in the $-x$-direction, towards the platform, to achieve a reflector illumination blockage error, as is illustrated in Fig. 8. The enclosing box RS in Fig. 6 was re-used for the antenna defect source reconstruction problem, resulting in the same number of input data points and unknowns as in the nominal case. The reconstructed equivalent electric current density components computed from the total far-field of the defect antenna scenario are presented in Fig. 9. When comparing the reconstructed currents in Fig. 7 and in Fig. 9 it is seen that the blockage of the reflector illumination has an effect on the reconstructed currents, especially in the co-polar scattering from the rightmost side of the platform in Fig. 9.

B. Ice cloud imager 664 GHz feed horn

Next, the method was evaluated for source reconstruction of high frequency applications, where measurement data of a 664 GHz feed horn was used as input. The antenna had been measured by ESA at the European space research and technology centre (ESTEC) sub-mm wave scanner in support to the ice cloud imager instrument of the MetOp-SG program [25]. During the experimental characterisation of the antenna under test (AUT) an WR1.5 open ended waveguide (OEW) with a conical shape for backscatter reduction was used as a probe. The co-polarisation and cross-polarisation near-fields were sampled over a planar scan surface of 20 mm x 20 mm located 2 mm in front of the AUT. Further details of the measurement campaign are presented in [25]. From the measured near-field data the far-field of the AUT was computed and provided to TICRA. Far-field data was only available in a truncated angular range in the forward hemisphere at the angles $\theta = [-75^\circ, 75^\circ]$. The sampling density of the provided far-field is 0.1° in θ and 22.5° in ϕ. Ideally, the data should have been sampled more densely in the ϕ-direction in order to fulfil the recommended sampling criterion for source reconstruction. To this end, a spherical wave expansion of the measured data was carried out as a preconditioning step to interpolate the measured data.

In order to carry out source reconstruction of the AUT knowledge of the physical envelope of the antenna is required. A sketch of the envelope of the AUT is presented in Fig. 10. A 15 mm x 15 mm x 22 mm box reconstruction surface was applied that encloses the AUT envelope, and provides some margin for AUT misalignments in the measurements, as is illustrated in Fig. 11. The computational details of the 664 GHz horn source reconstruction case are presented in Table I. The problem consists of 574 464 HO unknowns, it requires 6.0 GB of RAM and was computed in 44 minutes on the same 32 core computation machine as was used in Section V-A. A much smaller computer could of course have been used in the analysis of the problem, with the main difference that the computation time would have been longer.

The two polarisation components of the reconstructed elec-

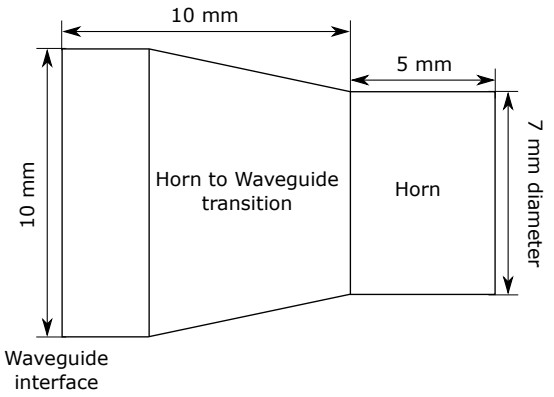

Fig. 10: Application case 2 envelope enclosing the AUT.

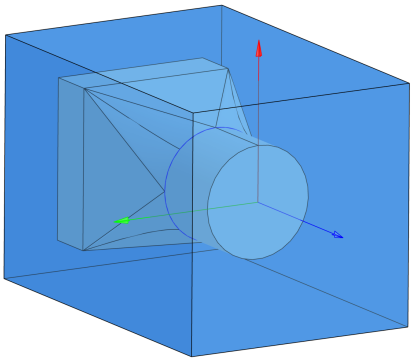

Fig. 11: Application case 2 AUT mock-up with the RS used in the source reconstruction analysis.

tric current density at the RS as seen from the AUT main beam direction are presented in Fig. 12. Since no prior information had been provided of the AUT radiation except for the far-field it was difficult to access the antenna performance solemnly based on the reconstructed currents. Nevertheless, the results indicate that the antenna performs as expected both in terms of the co-polarisation beam shape and the cross-polarisation levels and symmetry. In the same manner as for case 1, the reconstructed far-field was computed with the sampling $\theta = [0, 75]^\circ$, $N_\theta = 1001$, $\phi = [0, 315]^\circ$, $N_\phi = 8$. The resulting far-field RMSE was $< 0.3\,\%$ which shows that the input far-field had been successfully reconstructed by the source reconstruction solver.

C. Computational requirements

As a final step, source reconstruction of example case 1 in Section V-A and example case 2 in Section V-B were attempted using the 3D reconstruction method in DIATOOL 1.1, the most recent commercially available version of the software. The 3D reconstruction method in this software consists of a 3D MoM SCGLS solver, which represent the current state-of-the-art in terms of commercially available source reconstruction software. The main limitations of the SCGLS reconstruction method is the scaling of the memory

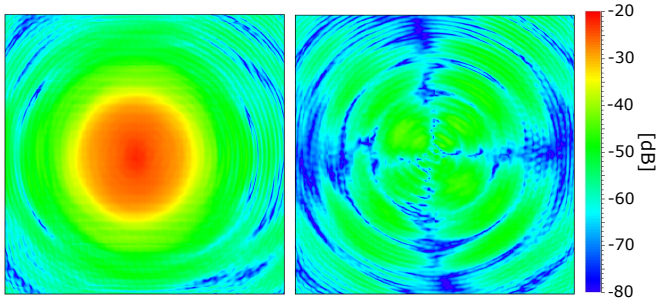

Fig. 12: Application case 2 reconstructed electric current density. The co-polarisation currents are presented to the left and the cross-polarisation currents to the right.

TABLE I: Analysis requirements of application cases 1 and 2, where the Calderón inverse 3D MoM method is compared to the previous state-of-the-art SCGLS inverse 3D MoM method.

Case	Solver	RS	Nbr. of unknowns	Memory req. (GB)	Comp. time (hh:mm)
1	Calderón	box	3 229 688	60	04:05
1	SCGLS	box	3 229 688	223 000	–:–
2	Calderón	box	574 464	6	00:44
2	SCGLS	box	574 464	6 660	–:–

requirements and simulation time in relation to the number of unknowns and the frequency of the AUT. For example, the simulation times scale with frequency as $\mathcal{O}(f^6)$. The values in Table I show that the high frequency horn example would require 6.66 TB of RAM to solve using SCGLS, and the reflector on platform example would require 223 TB of RAM. This comparison clearly displays the extreme acceleration that has been achieved in the new Calderón source reconstruction solver presented.

VI. Conclusion

An extremely efficient implementation of a fast source reconstruction method for radiating structures on electrically large platforms has been presented for the first time. The implementation demonstrates drastic reductions in memory requirement and computation time in relation to current state-of-the-art source reconstruction solvers. In particular, the implementation is to the authors' knowledge the first published matrix-free source reconstruction method with $\mathcal{O}(N \log N)$ complexity. The effect of this complexity reduction in practice is so substantial that the memory requirements are comparable to that of solving the forward radiation problem, a substantial feat in any inverse solver implementation. Crucially, as we have demonstrated, these computational improvements come with no significant loss of accuracy.

References

[1] E. Jørgensen, P. Meincke, C. Cappellin, and M. Sabbadini, "Improved source reconstruction technique for antenna diagnostics,," in *Proceeedings of the 32nd ESA Antenna Workshop*, ESTEC, Noordwijk, The Netherlands, 2010.

[2] L. Foged, L. Scialacqua, F. Saccardi, J. A. Quijano, G. Vecchi, and M. Sabbadini, "Practical application of the equivalent source method as an antenna diagnostics tool [amta corner]," *IEEE Antennas and Propagation Magazine*, vol. 54, no. 5, pp. 243–249, 2012.

[3] E. Jørgensen, P. Meincke, and C. Cappellin, "Advanced processing of measured fields using field reconstruction techniques," in *European Conference on Antennas and Propagation*, 2011, pp. 3880–3884.

[4] J. L. Araque Quijano, L. Scialacqua, J. Zackrisson, L. J. Foged, M. Sabbadini, and G. Vecchi, "Suppression of undesired radiated fields based on equivalent currents reconstruction from measured data," *IEEE Antennas and Wireless Propagation Letters*, vol. 10, pp. 314–317, 2011.

[5] T. F. Eibert, E. Kilic, C. Lopez, R. A. M. Mauermayer, O. Neitz, and G. Schnattinger, "Electromagnetic Field Transformations for Measurements and Simulations (Invited Paper)," *Progress In Electromagnetics Research*, vol. 151, pp. 127–150, 2015.

[6] L. Scialacqua, L. J. Foged, F. Mioc, and F. Saccardi, "Link between measurement and simulation applied to antenna scattering and placement problems," in *2017 11th European Conference on Antennas and Propagation (EUCAP)*, 2017, pp. 2951–2955.

[7] B. Xu, Z. Ying, L. Scialacqua, A. Scannavini, L. J. Foged, T. Bolin, K. Zhao, S. He, and M. Gustafsson, "Radiation performance analysis of 28 ghz antennas integrated in 5g mobile terminal housing," *IEEE Access*, vol. 6, pp. 48 088–48 101, 2018.

[8] J. L. A. Quijano and G. Vecchi, "Field and source equivalence in source reconstruction on 3d surfaces," *Progress In Electromagnetics Research*, vol. 103, pp. 67–100, 2010.

[9] A. E. H. Love, "The Integration of the Equations of Propagation of Electric Waves," *Philosophical Transactions of the Royal Society A*, vol. 197, pp. 1–43, Sep. 1901.

[10] L. J. Foged, L. Scialacqua, F. Saccardi, J. L. A. Quijano, and G. Vecchi, "Application of the Dual-Equation Equivalent-Current Reconstruction to Electrically Large Structures by Fast Multipole Method Enhancement [AMTA Corner]," *IEEE Antennas and Propagation Magazine*, vol. 56, no. 5, pp. 264–273, Oct. 2014.

[11] T. F. Eibert and C. H. Schmidt, "Multilevel Fast Multipole Accelerated Inverse Equivalent Current Method Employing Rao–Wilton–Glisson Discretization of Electric and Magnetic Surface Currents," *IEEE Transactions on Antennas and Propagation*, vol. 57, no. 4, pp. 1178–1185, Mar. 2009.

[12] T. F. Eibert, D. Vojvodic, and T. B. Hansen, "Fast Inverse Equivalent Source Solutions With Directive Sources," *IEEE Transactions on Antennas and Propagation*, vol. 64, no. 11, pp. 4713–4724, Oct. 2016.

[13] E. Jørgensen, O. Kim, P. Meincke, and O. Breinbjerg, "Higher order hierarchical legendre basis functions in integral equation formulations applied to complex electromagnetic problems," in *IEEE AP-S International Symposium*, vol. 3A, Washington DC, USA, jul 2005, pp. 64–67.

[14] O. Borries, "Regularization Methods for Computation of Equivalent Sources," Technical University of Denmark, Tech. Rep., Nov. 2011.

[15] J. Kornprobst, R. A. M. Mauermayer, E. Kilic, and T. F. Eibert, "An Inverse Equivalent Surface Current Solver with Zero-Field Enforcement by Left-Hand Side Calderón Projection," in *European Conference on Antennas and Propagation*, Krakow, Jan. 2019, pp. 1–3.

[16] S. Schelkunoff, "Some equivalence theorems of electromagnetics and their application to radiation problems," *Bell System Technical Journal*, vol. 15, pp. 92–112, 1936.

[17] DIATOOL Technical Specification, *S1493-TS*, TICRA, Copenhagen, Denmark, 2009.

[18] E. Jørgensen, P. Meincke, C. Cappellin, and M. Sabbadini, "Improved source reconstruction technique for antenna diagnostics," *Proceedings of the 32nd ESA Antenna Workshop, ESTEC, Noordwijk, The Netherlands*, 2010.

[19] E. Jørgensen, P. Meincke, and C. Cappellin, "Advanced processing of measured fields using field reconstruction techniques," *Proceedings of European Conference on Antennas and Propagation, EuCAP, Rome, Italy*, 2011.

[20] E. Jørgensen, P. Meincke, O. Borries, and M. Sabbadini, "Processing of measured fields using advanced inverse method of moments algorithm," *Proceedings of the 33rd ESA Antenna Workshop, ESTEC, Noordwijk, The Netherlands*, 2011.

[21] K. Persson and M. Gustafsson, "Reconstruction of equivalent currents using a near-field data transformation - with radome applications," *Progress in Electromagnetics Research*, vol. 54, pp. 179–198, 2005.

[22] J. L. A. Quijano and G. Vecchi, "Improved-accuracy source reconstruction on arbitrary 3-D surfaces," *IEEE Antennas and Wireless Propagation Letters*, vol. 8, pp. 1046–1049, 2009.

[23] C. Cappellin, "Antenna diagnostics for spherical near-field antenna measurements," ph.d. thesis, ISBN 97-887911-84802, Technical University of Denmark, Ørsted-DTU, Lyngby, Denmark, September 2007.

[24] P. E. Frandsen and M. Sabbadini, "An introduction to the electromagnetic data exchange language, issue 3," *http://www.antennasvce.org/Public/EDXP*, February 2009.

[25] E. Saenz, M. Paquay, L. Rolo, E. van der Houwen, P. Radzik, P. de Maagt, U. Klein, G. Sonnabend, and D. M. Alvarez, "Measurements of the 664 ghz feed horn for the ici instrument of the metop-sg satellite," in *2017 International Symposium on Antennas and Propagation (ISAP)*. IEEE, 2017, pp. 1–2.